

Elucidating Dark Energy with Future 21 cm Observations at the Epoch of Reionization

Kazunori Kohri^{1,2}, Yoshihiko Oyama³, Toyokazu Sekiguchi⁴
and Tomo Takahashi⁵

¹*The Graduate University for Advanced Studies (Sokendai),
1-1 Oho, Tsukuba 305-0801, Japan*

²*Institute of Particle and Nuclear Studies, KEK, 1-1 Oho, Tsukuba 305-0801, Japan*

³*Institute for Cosmic Ray Research, The University of Tokyo,
5-1-5 Kashiwanoha, Kashiwa, Chiba 277-8582, Japan*

⁴*Institute for Basic Science, Center for Theoretical Physics of the Universe,
Daejeon 34051, South Korea*

⁵*Department of Physics, Saga University, Saga 840-8502, Japan*

Abstract

We investigate how precisely we can determine the nature of dark energy such as the equation of state (EoS) and its time dependence by using future observations of 21 cm fluctuations at the epoch of reionization ($6.8 \lesssim z \lesssim 10$) such as Square Kilometre Array (SKA) and Omniscope in combination with those from cosmic microwave background, baryon acoustic oscillation, type Ia supernovae and direct measurement of the Hubble constant. We consider several parametrizations for the EoS and find that future 21 cm observations will be powerful in constraining models of dark energy, especially when its EoS varies at high redshifts.

1 Introduction

The origin of the present acceleration of the Universe has been one of the biggest mysteries in modern cosmology. To explain this acceleration, one can assume a mysterious component called dark energy [1] or, also resort to the modification of gravity [2]. Recently there have been attempts to describe these models using the effective field theory [3–5]. Another possible explanation such as late-time quantum backreaction from inflationary fluctuations has also been discussed [6–9].

A lot of efforts have also been made to elucidate the nature of dark energy by using cosmological observations. When one investigates the nature of dark energy using observational data, a phenomenological approach is often taken, in which the properties of dark energy, particularly, its equation of state (EoS) is parametrized in a general way. Since the EoS depends on time in most models of dark energy, its time evolution is usually accommodated when parametrizing it and constraints on such EoS parameters have been analyzed by using actual cosmological data (see [10] for the constraint from the measurement of cosmic microwave background (CMB) of Planck in combination with baryon acoustic oscillation (BAO), type Ia supernovae (SNe) and H_0 measurements for some parametrization, and [11] for a recent analysis). Although observational constraints on dark energy parameters are becoming more and more severe, we are still far from pinning down the model which describes the present-day cosmic acceleration. However because the accuracy of cosmological observations will be much improved in future, the nature of dark energy can be probed more accurately. Therefore it would be worth investigating how precisely we can obtain the information on dark energy parameters in future cosmological observations^{#1}.

As such, we in this paper focus on observations of fluctuations of 21 cm line of neutral hydrogen. Observations of 21 cm line can probe different redshift epochs compared with other methods. Therefore we can obtain unique information which cannot be acquired by other observations. In addition, the next generation of the 21 cm survey, Square Kilometre Array (SKA) [18], will be in operation in 2020s. Hence it is timely to study expected constraints on dark energy by using 21 cm experiments. There have been several works on dark energy using future observational data of 21 cm intensity mapping [19–22], HI galaxy survey [23] and 21 cm fluctuations [24–26]. In this paper, we use the 21 cm fluctuations to derive projected constraints on various dark energy models from SKA in combination with future CMB experiments such as COre+ [27] and future observations of SNe, BAO and a direct measurement of Hubble constant H_0 , assuming several types of dark energy parametrizations. As mentioned above, because the 21 cm observations can probe the different epochs of the dark energy evolution compared to other observations, it should be complementary to those of others. In addition to SKA, we also consider the next-next generation of the 21 cm experiment such as Omniscope [28], which is expected to give an unprecedented accuracy. By making an analysis adopting the above mentioned

^{#1} A lot of researches have been done in this direction, by adopting future observations of CMB, large scale structure and so on, see [12–17] for relatively recent works along this line.

observations, we discuss how the 21 cm observation can probe the nature of dark energy.

The organization of this paper is as follows. In the next section, we summarize how to parametrize dark energy EoS, which is used in this paper. Then in Section 3, we present current constraints on dark energy parameters introduced in Section 2. Then in Section 4, we investigate expected constraints on dark energy from future observations of 21 cm line in combination with other observations such as CMB, BAO, SNeIa and H_0 . The final section is devoted to the conclusion of this paper.

2 Dark energy parametrizations

In this section, we summarize parametrizations for dark energy equations of state w_X which are used in our analysis. In most models of dark energy, its EoS depends on time. However, the time variation of w_X is highly model-dependent, and thus it is customary to assume some parametrization for w_X to take the time-dependence into account. Although there have been proposed a lot of possible parametrizations, we adopt some representative ones in this paper. For some other parametrizations, see, for example, Ref. [29], in which various dark energy parametrizations are discussed. Behaviors of EoS $w_X(z)$ and the density parameter $\Omega_X(z)$ for the dark energy parametrizations adopted in this paper are shown in Fig. 1.

• Parametrization I

One of simple ways to parametrize the time-varying w_X is to assume that w_X varies linearly with the scale factor, which can be given by the following form [30, 31]:

$$w_X(z) = w_0 + (1 - a)w_1 = w_0 + \frac{z}{1+z}w_1, \quad (1)$$

where a and z are respectively the scale factor and redshift^{#2}. w_0 represents the EoS at present while $w_0 + w_1$ is its value at far past. With this parametrization, the energy density of dark energy can be given by

$$\rho_X(z) = \rho_{X0}(1+z)^{3(1+w_0+w_1)} \exp\left[-\frac{3w_1z}{1+z}\right], \quad (2)$$

with ρ_{X0} being the dark energy density at present.

• Parametrization II

In some models of dark energy, its EoS suddenly changes from some constant value to another. This kind of changes cannot be accommodated in the above parametrization.

^{#2} Another parametrization in which w_X changes linearly with the redshift has also been adopted in some literature [32–34]. However, here we do not consider such a parametrization.

The authors of [35] have introduced a parametrization which can represent this kind of sudden change of $w_X(z)$:

$$w_X(z) = w_0 w_1 \frac{a^p + a_s^p}{w_1 a^p + w_0 a_s^p} = w_0 w_1 \frac{1 + \left(\frac{1+z}{1+z_s}\right)^p}{w_1 + w_0 \left(\frac{1+z}{1+z_s}\right)^p}, \quad (3)$$

where $a_s(z_s)$ corresponds to the scale factor (redshift) at which w_X changes suddenly from w_1 to w_0 . In the above expression, p controls the width of the transition.

The time evolution of the dark energy density in this parametrization is calculated as

$$\rho_X(z) = \rho_{X0}(1+z)^{3(1+w_0)} \left(\frac{w_0 + w_1(1+z_s)^p}{w_0(1+z)^p + w_1(1+z_s)^p} \right)^{3(w_0-w_1)/p}. \quad (4)$$

• Parametrization III

A commonly assumed dark energy evolves in such a way that its energy density begins to dominate only at a late epoch of the Universe, and it is subdominant at an earlier time. However, in some models such as tracker quintessence model in which its EoS traces that of the dominant component in the Universe (i.e., radiation or matter). Such a model is sometimes called “early dark energy” since its energy density contributes to the total one to some extent. To represent this kind of models, the following parametrization has been proposed [36]:

$$w_X(z) = \frac{w_0}{[1 + b \log(1+z)]^2}, \quad (5)$$

where w_0 corresponds to the present-day equation of state. To avoid too large value (or divergence) of w_X at earlier times, b should be positive. Then, when $1+z$ is large, w_X approaches to 0, which is the same as that of matter. Therefore, this kind of dark energy can give some contribution at earlier times (in matter-dominated epoch). The energy density of dark energy of this parametrization can be written as

$$\rho_X(z) = \rho_{X0}(1+z)^{3(1+\alpha_X(z))}, \quad (6)$$

where

$$\alpha_X(z) = \frac{w_0}{1 + b \log(1+z)}. \quad (7)$$

3 Current constraints

Before investigating the future expected constraints on dark energy parameters, here we study constraints from current observations such as Planck, BAO, SNeIa, H_0 and weak lensing for each parametrization. Although similar analyses have been done in the literature for some parametrizations, we update those constraints, and by doing those analyses,

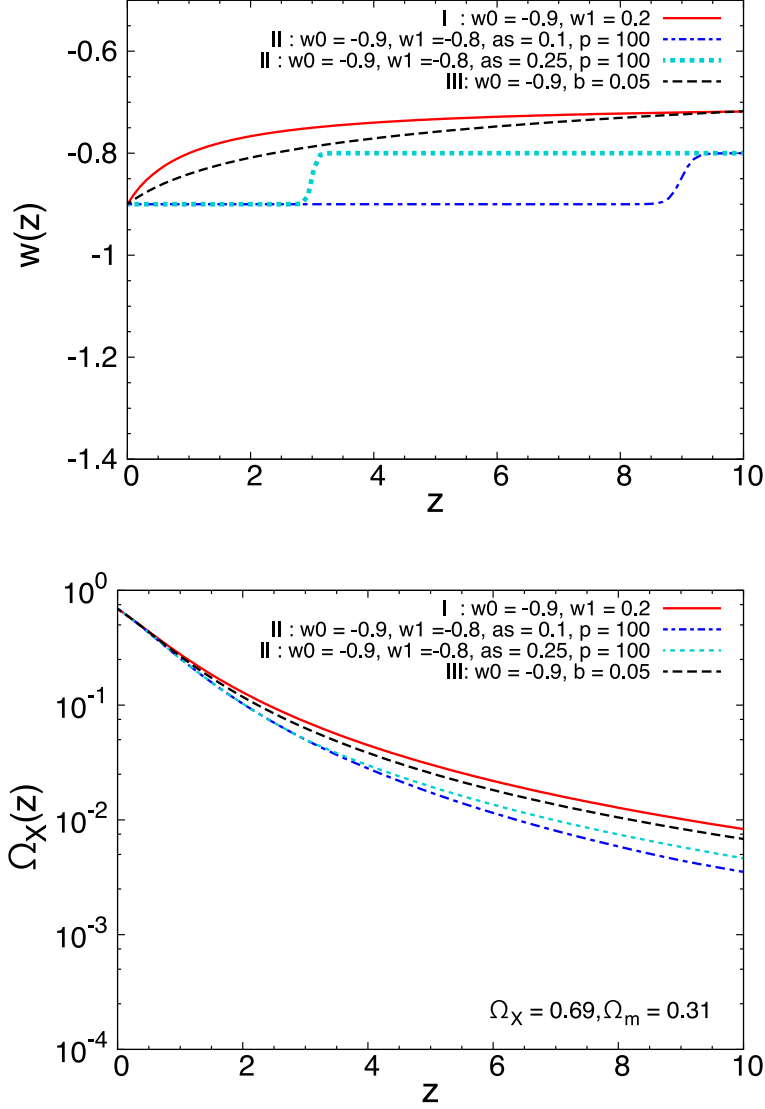


Figure 1: Time evolutions of EoS $w(z)$ (upper panel) and the density parameter $\Omega_X(z)$ (lower panel) for the dark energy parametrizations considered in this paper. The labels I, II and III indicate the parameterization I, II and III, respectively. For the values of the parameters in each parameterization, we assumed the same ones as in Table. 2 .

we can choose fiducial values for the EoS parameters consistent with current observational data in the next section.

We have performed Markov Chain Monte Carlo (MCMC) analyses by using a modified version of CosmoMC [37], in which we have accommodated the dark energy parametrizations introduced in Section 2. For the sound speed c_s^2 which needs to be specified when solving the perturbation equations, we fixed it as $c_s^2 = 1$ in the analysis of this section. In addition to the dark energy parameters, we have also varied the standard cosmological parameters: baryon density $\Omega_b h^2$, dark matter density $\Omega_{\text{DM}} h^2$, the amplitude and the spectral index of the scalar mode primordial power spectrum A_s and n_s , the reionization optical depth τ and the acoustic peak scale θ_s . Here h is the normalized Hubble parameter defined as $H_0 = 100h$ km/sec/Mpc.

In deriving constraints from current data, we adopt two different data sets. The first one is “Planck+BAO+lensing” which includes the power spectra of the CMB temperature and polarization anisotropies (TT+TE+EE at $\ell \geq 30$ and TT+TE+EE+BB at $\ell \leq 29$) from Planck [38], BAO scales in galaxy power spectrum [39–41] and the Planck CMB lens power spectrum [42]. The other data set we adopt in this analysis is “Planck+BAO+lensing+ H_0 +SN+WL” in which data from measurements of Hubble constant $H_0 = 70.6 \pm 3.3$ km/s/Mpc [43], the JLA compilation of type Ia supernovae [44] and the CHFTLenS cosmic shear power spectrum [45] are added to “Planck+BAO+lensing.”

In Figs. 2, 3 and 4, we present the constraints for the parametrizations I, II and III, respectively. For the parametrization I, we have assumed the prior for the EoS parameters w_0 and w_1 as $-3 \leq w_0 \leq 1$ and $-3 \leq w_1 \leq 3$, respectively. The constraint on this parametrization has been investigated in [10], using almost the same (but slightly different) data sets. Our result is consistent with the one obtained in [10]. For the parametrization II, we have fixed a_s and p and show the constraints on the w_0 – w_1 plane. In Fig. 3, we present our results for the cases with $(a_s, p) = (0.5, 1)$ (left panel) and $(a_s, p) = (0.5, 100)$ (right panel). The prior for w_0 and w_1 are assumed as $-3 \leq w_0 \leq 1$ and $-3 \leq w_1 \leq 3$, as in the case for the parametrization I. The constraints on this parametrization has been studied by using Planck and BAO in [46]. For the parametrization III, we have only two parameters for EoS, w_0 and b . Therefore we show the constraint on the w_0 – b plane for this parametrization. As stated in the previous section, this parametrization captures the property of the so-called early dark energy models. In [10], the early dark energy model been studied, but with a different parametrization from the one adopted here. Yet another parametrization of early dark energy has also been discussed in [47] by using Planck 2013 data.

Having obtained the current constraints on the parameters for EoS, we choose fiducial values of the EoS parameters, which are allowed within at 2σ level, in order to perform the Fisher matrix analysis in the next section.

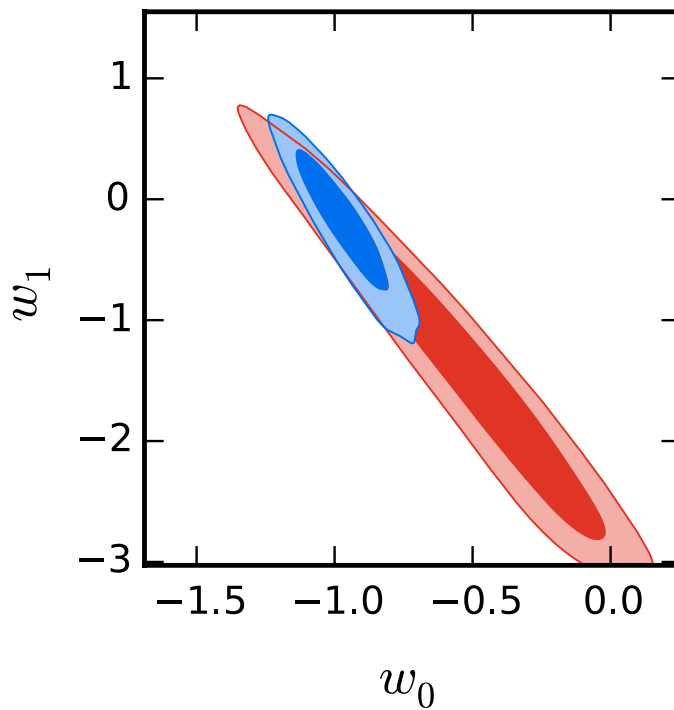


Figure 2: Current constraint on the parametrization I in the w_0 - w_1 plane. We show the constraints from Planck+BAO+lensing (red region) and Planck+BAO+lensing+ H_0 +SNe+WL (blue region). The dark and the light colors correspond to 1σ and 2σ allowed regions, respectively.

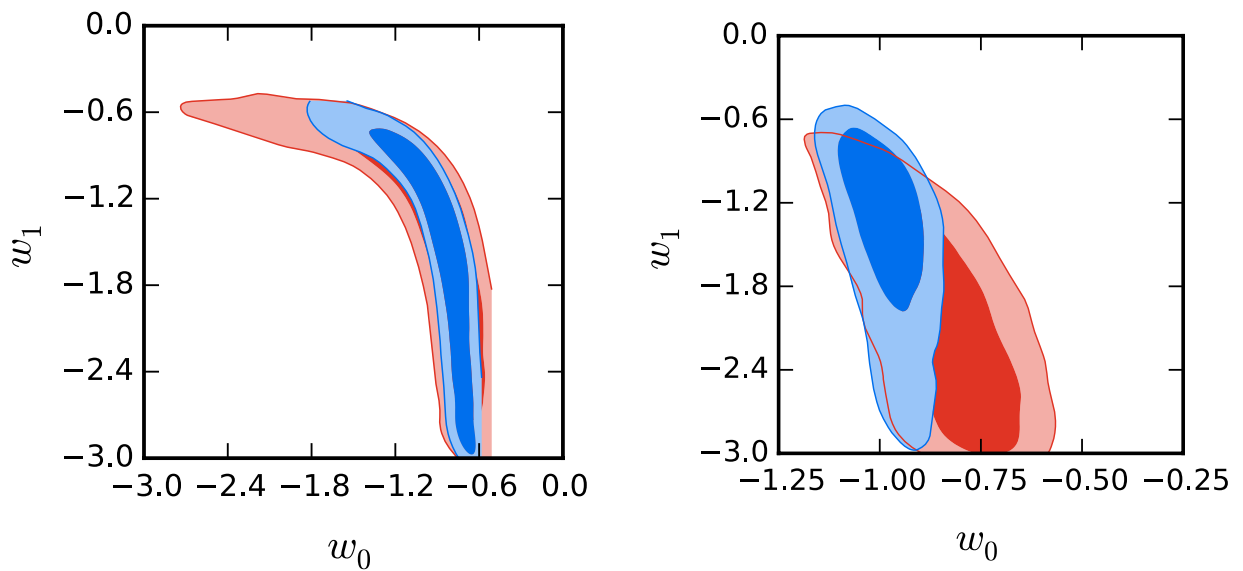


Figure 3: The same as Fig. 2, but for the parametrization II in the w_0 - w_1 plane. We show the cases of $p = 1$ at the left panel, and $p = 100$ at the right panel, respectively. We chose $a_s = 0.5$ commonly in the both panels.

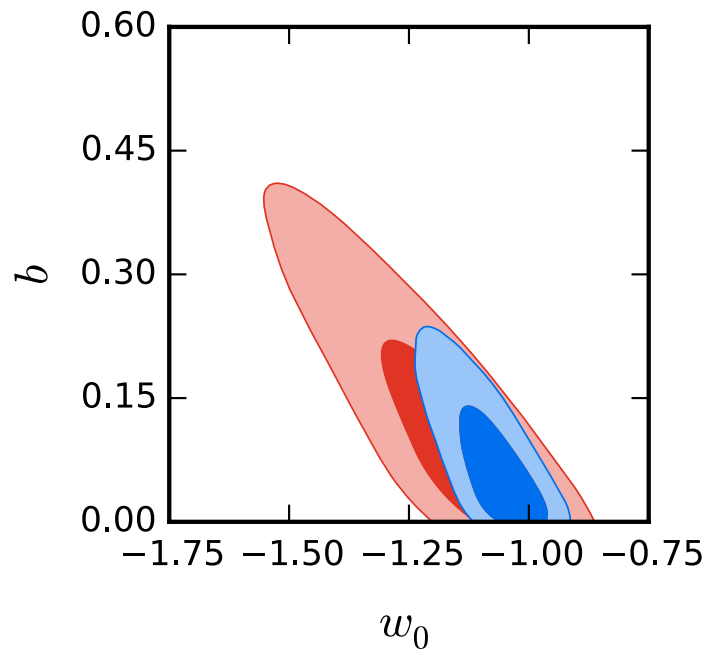


Figure 4: The same as Fig. 2, but for the parametrization III in the w_0 - b plane.

4 Future expected constraints

Now in this section, we present the expected constraints from future 21 cm experiments such as SKA and Omniscopes in combination with future CMB observations such as COrE+. For comparison, we also show the results with the specification of Planck. In addition, we combine future observations of SNe, BAO and direct Hubble constant measurement to obtain the expected constraints. For this purpose, we adopt the Fisher matrix analysis. The specifications of observations assumed in this paper are summarized in Appendix A. Since the method of the Fisher analysis for the 21cm fluctuations and CMB adopted in this paper is the same as the one in our previous paper [48], here we just briefly summarize them. For the details, we refer the readers to [48, 49]. We also briefly describe our methods for the analysis of future observations of SNe, BAO and the direct Hubble constant measurement. After summarizing our methods for the Fisher analysis, we present our results on the expected constraints on dark energy parameters for each parametrization in order.

In our Fisher analysis, the fiducial values of the cosmological parameters are set to the mean values from the analysis of Planck TT,TE,EE+lowP+lensing+ H_0 +SNe+BAO [69]: $\Omega_b h^2 = 0.0223$, $\Omega_m h^2 = 0.1417$, $\Omega_X = 0.6911$, $\tau = 0.066$, $A_s 10^{10} = 21.42$ and $n_s = 0.9667$, and $Y_p = 0.25$, where Y_p is the primordial ${}^4\text{He}$ mass fraction. In our analysis, the total mass of neutrinos is fixed as $\Sigma m_\nu = 0.06$ eV, and we assume that the hierarchy of the masses is normal ordering. For the EoS parameters, we choose multiple sets for each parametrization.

4.1 21cm

The Fisher matrix for 21 cm fluctuations is given by

$$F_{ij}^{(21\text{cm})} = \sum_{\text{pixels}} \frac{1}{(\delta P_{21}(\mathbf{u}))^2} \frac{\partial P_{21}(\mathbf{u})}{\partial p_i} \frac{\partial P_{21}(\mathbf{u})}{\partial p_j}, \quad (8)$$

where $P_{21}(\mathbf{u})$ and $\delta P_{21}(\mathbf{u})$ are the 21 cm power spectrum and its error in \mathbf{u} space, respectively, and $p_i(p_j)$ represents cosmological parameters. Here \mathbf{u} is the Fourier dual of

$$\Theta = \theta_x \hat{e}_x + \theta_y \hat{e}_y + \Delta f \hat{e}_z = \Theta_\perp + \Delta f \hat{e}_z, \quad (9)$$

where Θ_\perp is the measured angular position on the sky and Δf represents the frequency which is given by the difference from the central redshift of a given bin. By adopting the flat-sky approximation, \mathbf{u} can be related to \mathbf{k} which is the Fourier dual to the position vector \mathbf{r} as [48, 49]

$$\mathbf{u}_\perp = d_A(z) \mathbf{k}_\perp, \quad u_\parallel = y(z) k_\parallel, \quad (10)$$

where $d_A(z)$ is the angular diameter distance to the redshift z and $y(z) = \lambda_{21}(1+z)^2/H(z)$ with λ_{21} being the wavelength of 21 cm line. A vector with the subscript \perp (\parallel) denotes

the component perpendicular (parallel) to the line of sight. From the above formulas, the power spectra in \mathbf{u} -space and \mathbf{k} -space are related as

$$P_{21}(\mathbf{u}) = \frac{1}{d_A(z)^2 y(z)} P_{21}(\mathbf{k}). \quad (11)$$

The power spectrum $P_{21}(\mathbf{k})$ is defined by

$$\langle \delta T_b(\mathbf{k}) \delta T_b^*(\mathbf{k}') \rangle = (2\pi)^3 \delta^{(3)}(\mathbf{k} - \mathbf{k}') P_{21}(\mathbf{k}), \quad (12)$$

where $\delta T_b(\mathbf{k})$ is fluctuations of the differential brightness temperature of the 21 cm line (T_b) relative to that of CMB (T_{cmb}). T_b in the position space is given by

$$T_b(\mathbf{x}) = \bar{T}_b (1 - \bar{x}_i (1 + \delta_x(\mathbf{x}))) (1 + \delta(\mathbf{x})) \left(1 - \frac{1}{aH} \frac{dv_r}{dr} \right), \quad (13)$$

where barred quantities represent their averaged ones, and here we have assumed $T_s \gg T_{\text{cmb}}$ with T_s the spin temperature since we consider the reionization era in this paper. \bar{T}_b is the average brightness temperature, which can be written as

$$\bar{T}_b \simeq 27 \bar{x}_H \left(\frac{1 - Y_p}{1 - 0.25} \right) \left(\frac{\Omega_b h^2}{0.022} \right) \left(\frac{0.14}{\Omega_m h^2} \frac{1+z}{10} \right)^{1/2} \text{ mK}, \quad (14)$$

where x_H is the neutral hydrogen fraction. δ_x and δ are fluctuations of the ionization fraction $x_i = 1 - x_H$ and the hydrogen number density n_H , respectively. $(1/aH)(dv_r/dr)$ represents the peculiar velocity and can be treated as a perturbation, which we define to be $\delta_v(\mathbf{x}) \equiv (1/aH)(dv_r/dr)$. The Fourier transform of $\delta_v(\mathbf{x})$ is related to $\delta(\mathbf{k})$ as $\delta_v(\mathbf{k}) = -\mu^2 \delta(\mathbf{k})$ with $\mu = \hat{\mathbf{k}} \cdot \hat{\mathbf{n}}$ being the cosine of the angle of \mathbf{k} relative to the line of sight. Since the fluctuations of T_b is given by $\delta T_b(\mathbf{x}) = T_b(\mathbf{x}) - \bar{T}_b$, the power spectrum in the \mathbf{k} -space can be written as

$$P_{21}(\mathbf{k}) = [\mathcal{P}_{\delta\delta}(k) - 2\mathcal{P}_{x\delta}(k) + \mathcal{P}_{xx}(k)] + \mu^2 [2\mathcal{P}_{\delta\delta}(k) - 2\mathcal{P}_{x\delta}(k)] + \mu^4 \mathcal{P}_{\delta\delta}(k), \quad (15)$$

where $k = |\mathbf{k}|$, $\mathcal{P}_{\delta\delta} = \bar{T}_b^2 P_{\delta\delta}$, $\mathcal{P}_{x\delta} = \bar{T}_b^2 (\bar{x}_i / \bar{x}_H) P_{x\delta}$ and $\mathcal{P}_{xx} = \bar{T}_b^2 (\bar{x}_i^2 / \bar{x}_H^2) P_{xx}$ with $P_{\delta\delta}$, $P_{x\delta}$ and P_{xx} being the power spectra for δ and δ_x defined as the same as that for P_{21} given in Eq. (12). Here $P_{\delta\delta}$ represents the matter fluctuations which carries the information of cosmology, and hence can probe the nature of dark energy. $P_{x\delta}$ and P_{xx} are the power spectra involving δ_x . After the reionization has started, these power spectra can significantly affect the total 21 cm power spectrum, and they are determined by the physics of reionization. For these power spectra, here we assume the following forms which can be well fitted by a result from radiative transfer simulations of [50, 51]:

$$\mathcal{P}_{xx}(k) = b_{xx}^2 [1 + \alpha_{xx}(kR_{xx}) + (kR_{xx})^2]^{-\gamma_{xx}/2} \mathcal{P}_{\delta\delta}(k), \quad (16)$$

$$\mathcal{P}_{x\delta}(k) = b_{x\delta}^2 e^{-\alpha_{x\delta}(kR_{x\delta}) - (kR_{x\delta})^2} \mathcal{P}_{\delta\delta}(k). \quad (17)$$

The amplitudes and the shapes of the spectra are described by the parameters $b_{xx}, b_{x\delta}, \alpha_{xx}, \gamma_{xx}$ and $\alpha_{x\delta}$, and $R_{xx}, R_{x\delta}$ are the parameters characterizing the effective size of the ionized bubbles. In our Fisher analysis, we also vary these ionization parameters, but marginalize over them to obtain expected constraints on dark energy parameters. For the fiducial values, we assume the same ones which are given in Table III of [49] (or Table 1 of [48]). In our analysis, we divide the redshift bins into four: $z = 6.75 - 7.25, 7.25 - 7.75, 7.75 - 8.25$ and $8.25 - 10.05$.

The error power spectrum $\delta P_{21}(\mathbf{u})$ is given by

$$\delta P_{21}(\mathbf{u}) = \frac{P_{21}(\mathbf{u}) + P_N(u_\perp)}{N_c^{1/2}}, \quad (18)$$

where $P_N(u_\perp)$ is the noise power spectrum, and the first term in the RHS represents the sample variance. The quantities to describe P_N are summarized in Table 1. In order to avoid the foreground contamination, we do not use the wavelength less than $k_{\min\parallel} = 2\pi/(yB)^{\#3}$, where B is the band width. We also cut the wavelength larger than $k_{\max} = 2 \text{ Mpc}^{-1}$ not to be affected by non-linear effect.

Noise power spectrum:	$P_N(u_\perp) = \left(\frac{\lambda^2(z) T_{\text{sys}}(z)}{A_e(z)} \right)^2 \frac{1}{t_0 n(u_\perp)}$
System temperature:	$T_{\text{sys}} = T_{\text{sky}} + T_{\text{rcvr}}$
Sky temperature:	$T_{\text{sky}} = 60 (\lambda/[m])^{2.55}$
Receiver noise:	$T_{\text{rcvr}} = 0.1 T_{\text{sky}} + 40[\text{K}]$
Number of independent cells:	$N_c = 2\pi k_\perp \Delta k_\perp \Delta k_\parallel V(z)/(2\pi)^3$
Survey volume:	$V(z) = d_A(z)^2 y(z) B \times \text{FoV}$
Effective collecting area:	A_e
Observation time:	t_0
Number density of the baseline:	$n(u_\perp)$
Field of view:	FoV

Table 1: Quantities to describe the error power spectrum P_N .

The methodology described above is basically the same as the one adopted in [48]. Since the publication of [48] however, the specification of SKA has been changed. Hence we adopt the new specification and summarize it in Table A.3 in Appendix A.

^{#3} Although we simply remove the modes with this criterion, the foreground could leak to the so-called “foreground wedge,” which can be a serious problem in deriving the constraints [52–61]. To estimate the impact of the foreground wedge on our results, we have also made the analysis by removing the modes with $\mu < \mu_{\min} = k_\parallel / \sqrt{k_\perp^2 + k_\parallel^2}$ [62], where μ_{\min} can be ~ 0.95 at $z \sim 8$. For such a value of μ_{\min} , we found that the error can become larger by a bit less than a factor of 2 in some particular cases. However, we note that even in such a case, the constraints can be improved by adding the information of 21cm.

We also note here that, in the following analysis, we focus on the 21 cm signals of redshift ranges $6.8 < z < 10$, which corresponds to the era of reionization, and investigate how such high redshift information can be useful to probe the nature of dark energy. Although 21 cm signals at low redshifts after reionization would also be very helpful [63–65], in this paper we focus on the 21 cm signals only at high redshifts.

Number density of the baseline: To set the number density of the baseline $n(u_\perp)$, we assume an azimuthally symmetric distribution for the antenna stations and adopt the following density profile which is consistent with the specification of the originally planned SKA1 [48]:

$$\rho(r) = \begin{cases} \rho_0 r^{-1}, & \rho_0 \equiv \frac{13}{16\pi(\sqrt{10}-1)} \text{ m}^{-2} & r \leq 400 \text{ m}, \\ \rho_1 r^{-3/2}, & \rho_1 \equiv \rho_0 \times 400^{1/2}, & 400 \text{ m} < r \leq 1000 \text{ m}, \\ \rho_2 r^{-7/2}, & \rho_2 \equiv \rho_1 \times 1000^2, & 1000 \text{ m} < r \leq 1500 \text{ m}, \\ \rho_3 r^{-9/2}, & \rho_3 \equiv \rho_2 \times 1500, & 1500 \text{ m} < r \leq 2000 \text{ m}, \\ \rho_4 r^{-17/2}, & \rho_4 \equiv \rho_3 \times 2000^4, & 2000 \text{ m} < r \leq 3000 \text{ m}, \end{cases} \quad (19)$$

where r is a radius from the center of the array. 95% of the stations are assumed to be in the region with $r < 3000$ m.

Although the original plan of SKA1 has assumed 911 antenna stations, in our analysis, we take the number of stations consistent with the re-baseline design of SKA in which $N_{\text{ant}} = 911/2$ for SKA1 and $N_{\text{ant}} = 911 \times 4$ for SKA2 as shown in Table A.3. Therefore the number density of the baseline $n(u_\perp)$ can be evaluated as

$$n_{\text{SKA1}}(u_\perp) = n_{\text{origSKA1}}(u_\perp) \times \left(\frac{1}{2}\right)^2, \quad (20)$$

$$n_{\text{SKA2}}(u_\perp) = n_{\text{origSKA1}}(u_\perp) \times 4^2, \quad (21)$$

where $n_{\text{origSKA1}}(u_\perp)$ is the number density of the baseline for the original design of SKA1 which is evaluated by its density profile of Eq. (19). $n_{\text{SKA1}}(u_\perp)$ and $n_{\text{SKA2}}(u_\perp)$ are the ones for SKA1 and SKA2, respectively. For Omniscope, we assume the same one as Ref. [49].

4.2 CMB

The Fisher matrix of CMB is written as

$$F_{ij}^{(\text{CMB})} = \sum_l \left(\frac{2l+1}{2}\right) f_{\text{sky}} \text{Tr} \left[\mathbf{C}_l^{-1} \frac{\partial \mathbf{C}_l}{\partial p_i} \mathbf{C}_l^{-1} \frac{\partial \mathbf{C}_l}{\partial p_j} \right], \quad (22)$$

where $p_i(p_j)$ represents cosmological parameters, and \mathbf{C}_l is the covariance matrix of CMB which is given by

$$\mathbf{C}_l = \begin{pmatrix} C_l^{TT} + N_l^T & C_l^{TE} & C_l^{Td} \\ C_l^{TE} & C_l^{EE} + N_l^P & 0 \\ C_l^{Td} & 0 & C_l^{dd} + N_l^d \end{pmatrix}, \quad (23)$$

where C_l^X is the angular power spectrum for unlensed CMB ($X = TT, TE, EE$), weak lensing deflection angle field ($X = dd$) and cross correlation between TT and d ($X = Td$). N_l^Y is the noise power spectrum which is given by

$$N_l^Y(\nu) = \Delta_Y^2 \exp [l(l+1)\sigma_b^2(\nu)], \quad (24)$$

where Δ_Y is the experimental noise, and $\sigma_b = \theta_{\text{FWHM}}/\sqrt{8 \ln 2}$ represents the beam width. When the multiple frequency channels are used, the total noise power spectrum can be provided by

$$(N_l^Y)^{-1} = \sum_{\nu_i} \frac{1}{N_l^Y(\nu_i)}. \quad (25)$$

For the noise power spectrum for weak lensing deflection angle N_l^d , we use FUTURCMB code [66] which adopts the quadratic estimator for lensing reconstruction [67]. f_{sky} is the fraction of the sky measured and we assume $f_{\text{sky}} = 0.65$.

For the specifications of CMB, we assume CORe+ and Planck. Although the specification of CORe+ can be found in [68], it is considered to be the one at the planning stage. Therefore, we use the values from Ref. [27], which is the original specification of CORe. Although the specification adopted in this work is a little bit different from the one assumed in [48], it does not change our results at all. We tabulate its specification in Table A.4. For Planck, we assume the same specification as that in [48].

4.3 BAO, SNe and Hubble constant

Here we describe our method of the analysis to obtain joint constraints from CMB, 21cm fluctuations, BAO, SNe and direct measurements of the Hubble constant H_0 . As mentioned above, the methods to analyze CMB and 21 cm fluctuations are the same as the one adopted in [48]. However, future observations of BAO, SNe and H_0 were not included in [48], and therefore, before showing our results on future constraints, we summarize formalisms of our analysis for BAO, SNe and H_0 (for reference, see also Refs. [70–72]).

4.3.1 BAO

Observations of BAO can probe the comoving angular diameter distance $d_A(z)$ and the Hubble parameter $H(z)$, which depend on underlying cosmological models. Therefore they are also affected by the EoS of dark energy. For our analysis, $\ln(d_A(z))$ and $\ln(H(z))$ are treated as observables and the Fisher matrix for BAO is given by

$$\begin{aligned} F_{\alpha,\beta}^{(\text{BAO})} &= F_{\alpha,\beta}^{(\text{BAO}),d} + F_{\alpha,\beta}^{(\text{BAO}),H} \\ &= \sum_i \frac{1}{\sigma_d^2(z_i)} \frac{\partial \ln(d_A(z_i))}{\partial \theta_\alpha} \frac{\partial \ln(d_A(z_i))}{\partial \theta_\beta} + \sum_i \frac{1}{\sigma_H^2(z_i)} \frac{\partial \ln(H(z_i))}{\partial \theta_\alpha} \frac{\partial \ln(H(z_i))}{\partial \theta_\beta}, \end{aligned} \quad (26)$$

where the sum should be performed for the redshift bins whose width, and its central value for the i -th bin are denoted as Δz_i and z_i , respectively^{#4}. $\sigma_d(z_i)$ and $\sigma_H(z_i)$ are errors of $\ln(d_A(z_i))$ and $\ln(H(z_i))$ at each redshift bin. θ_α (and θ_β) represents the cosmological parameters which are relevant to observations of BAO: $\Omega_m h^2$, Ω_X ^{#5} and the dark energy EoS parameters. The component $F_{\alpha,\beta}$ which are irrelevant to the BAO observables are set to be zero.

In the following analysis, for a future BAO observation, we adopt the specification of Dark Energy Spectroscopic Instrument (DESI) [74, 75]. We assume the redshift range, bins and expected errors for $\ln(d_A(z_i))$ and $\ln(H(z_i))$ as the same as those given in Table 5 of [74].

4.3.2 Direct measurement of H_0

In future, direct measurement of the Hubble constant H_0 will be more precise to reach the level of 1 % [76–78]. Here we assume that we can determine the Hubble constant at a 1 % accuracy in our analysis, which is expressed in the Fisher matrix to be [79]

$$F_{\alpha,\beta}^{(H_0)} = \frac{1}{(0.01 \times h_{\text{fid}})^2} \delta_{\alpha,h} \delta_{\beta,h}. \quad (27)$$

The Kronecker delta symbols indicate that the Fisher matrix component of (h, h) is the only nonzero entity in the Fisher matrix.

However, in fact, in our analysis, we do not adopt h as a primary parameter, but it is derived from other cosmological parameters. Hence we need to convert the Fisher matrix Eq. (27) to that for our primary cosmological parameters. Among the primary parameters adopted in our analysis, $\Omega_m h^2$ and Ω_X are relevant to h , and therefore, we transform the Fisher matrix with $(\alpha, \beta) = (h, \Omega_X)$ to the one with $(\alpha, \beta) = (\Omega_m h^2, \Omega_X)$ by using the following transformation [80]:

$$\tilde{F}_{l,m} = \frac{\partial \theta_j}{\partial \tilde{\theta}_l} \frac{\partial \theta_k}{\partial \tilde{\theta}_m} F_{jk}, \quad (28)$$

from which we obtain

$$\tilde{F}_{\alpha,\beta}^{(H_0)} = \begin{pmatrix} \tilde{F}_{\Omega_m h^2, \Omega_m h^2} & \tilde{F}_{\Omega_m h^2, \Omega_X} \\ \tilde{F}_{\Omega_m h^2, \Omega_X} & \tilde{F}_{\Omega_X, \Omega_X} \end{pmatrix} = \frac{1}{(0.01 \times h_{\text{fid}})^2} \begin{pmatrix} 1 \\ 2\Omega_m h^2 \end{pmatrix}^2 \begin{pmatrix} h^2 & h^4 \\ h^4 & h^6 \end{pmatrix}. \quad (29)$$

We use this Fisher matrix to incorporate a future observation of direct measurement of the Hubble constant in the following analysis.

^{#4} In general, measurements of d_A and H from BAO are correlated, and it should give rise to off-diagonal components in the covariant matrix that are omitted in Eq. (26). According to an analytical estimation [73], the correlation coefficients can be as large as 0.4. However, we find that the impact of the off-diagonal components at this level on the constraints of cosmological parameters are fairly small (only about 4-5%) in our results.

^{#5} We can also take h and Ω_X as the primary parameters for the analysis when we assume a flat Universe. However, in our analysis, we treat $\Omega_m h^2$ and Ω_X as the primary parameters.

4.3.3 Supernovae

Here we describe our method of the Fisher matrix analysis for SNe. For details, we refer the readers to [80, 81]. Observations of SNe probe the apparent magnitude m for each SNe which is related to the absolute magnitude M by the following relation:

$$m = M + \mu(z), \quad (30)$$

where $\mu(z)$ is the distance modulus and is related to the luminosity distance $d_L(z)$ as follows:

$$\mu(z) = 5 \log_{10} \left(\frac{d_L(z)}{\text{Mpc}} \right) + 25. \quad (31)$$

In a flat Universe, the luminosity distance is given by

$$d_L(z) = (1+z) \int_0^z \frac{d\bar{z}}{H(\bar{z})}. \quad (32)$$

Since the mean apparent magnitudes m of each bin are the observable, the Fisher matrix for SNe is written as

$$F_{\alpha,\beta}^{(\text{SN})} = \sum_i \frac{1}{\sigma_{\text{tot},i}^2} \frac{\partial m(\bar{z}_i)}{\partial \theta_\alpha} \frac{\partial m(\bar{z}_i)}{\partial \theta_\beta}, \quad (33)$$

$$\sigma_{\text{tot},i} = \sqrt{\sigma_{\text{stat},i}^2 + \sigma_{\text{sys},i}^2}, \quad (34)$$

where \bar{z}_i is the mean redshift for the i -th bin and $\sigma_{\text{tot},i}$, $\sigma_{\text{stat},i}$ and $\sigma_{\text{sys},i}$ are the total, statistical and systematic uncertainties for apparent magnitude, respectively. The statistical error $\sigma_{\text{stat},i}$ in a redshift bin consists of several components and is then

$$\sigma_{\text{stat},i} = \frac{1}{N_i} \sqrt{\sigma_{m,i}^2 + \sigma_D^2 + \sigma_{\text{lens},i}^2}, \quad (35)$$

where N_i is the number of SNe for the i -th bin, $\sigma_{m,i}$ is the photometric measurement error per supernova, σ_D is the intrinsic dispersion in luminosities of SNe, and $\sigma_{\text{lens},i}$ is the contribution of gravitational lensing magnifications. Here, we assume Gaussian uncertainties, and thus we add in quadrature these errors in the Fisher matrix above.

In our analysis, we use the specification of WFIRST-AFTA in Ref. [82], which is listed in Table A.6. For all bins including a near sample, we assume the common values for the measurement and intrinsic errors as $\sigma_{m,i} = 0.08$ and $\sigma_D = 0.09$. For the contribution of gravitational lensing $\sigma_{\text{lens},i}$, it is modeled as $\sigma_{\text{lens},i} = 0.07 \times \bar{z}_i$. Furthermore, we assume the systematic error per bin is given by $\sigma_{\text{sys},i} = 0.01 \times (1 + \bar{z}_i)/1.8$.

In observations of SNe, the absolute magnitude M is treated as a nuisance parameter and marginalized away to reduce the Fisher matrix for the cosmological parameter set. This procedure means that the Hubble constant h cannot be determined from SNe, and it would be redundant to take $\Omega_m h^2$ as a primary parameter. In our analysis therefore, we remove $\Omega_m h^2$ from a primary parameter but only Ω_X , and the dark energy EoS parameters are treated as primary ones for the Fisher matrix of SNe.

4.4 Future constraints on dark energy parameters

4.4.1 Parametrization I

Since there are only two parameters for the EoS in this parametrization, i.e., w_0 and w_1 , we show expected constraints on the w_0 - w_1 plane. In Fig. 5, we show parameter regions allowed at 95 % C.L. where we used CMB, BAO, SNe and H_0 with SKA1, SKA2 and Omniscope. For CMB, we performed the analysis by adopting the specifications of Planck and COrE+. The fiducial values for the EoS parameters are assumed to be $w_0 = -0.9$ and $w_1 = 0.2$ in Fig. 5, and $(w_0, w_1) = (-0.9, 0.05), (-0.95, 0.2), (-1.1, -0.2)$ in Fig. 6, respectively. We also need to specify the effective sound speed of dark energy c_s^2 to follow the evolution of the linear perturbations^{#6}, which are taken to be $c_s^2 = 1$ or $c_s^2 = 0$ in Fig. 5. By comparing the constraints for the cases with $c_s^2 = 1$ and 0, one finds that they are almost the same regardless of the value of c_s^2 , which indicates that the effects of varying c_s^2 is very weak, and its assumption scarcely affects the constraints. This also indicates that the nature of dark energy perturbation cannot be well probed by CMB nor 21 cm fluctuations, at least for dark energy models with this parametrization, and the constraints mainly comes from its effects on the background evolution.

In Fig. 6, expected constraints are shown for the fiducial values of $(w_0, w_1) = (-0.9, 0.05)$ (top), $(-0.95, 0.2)$ (middle) and $(-1.1, -0.2)$ (bottom) with the sound speed being fixed to be $c_s^2 = 1$. As seen from Figs. 5 and 6, when we add information from the 21 cm fluctuations, the constraints in this parametrization cannot be so drastically improved for SKA1 and SKA2, but can be done significantly for Omniscope. We should stress that the tendency depends on the parametrization as we discuss in the following sections. However, for the parametrization I, although the 21 cm observations look at different redshift range from CMB and other observations, and can probe multiple redshift slices, we need a better specification at the level of Omniscope to obtain a severe constraint on dark energy parameters.

4.4.2 Parametrization II

This parametrization includes four parameters to describe the EoS: w_0, w_1, a_s and p . To present our results, we show the constraints on 2D planes fixing or marginalizing other parameters. First we show the expected constraints on the w_0 - w_1 plane in the cases of $p = 100$ in Fig. 7, and $p = 1$ in Fig. 8. In each figure, we take several values for a_s to be $a_s = 0.5, 0.25, 0.1$ and assume the fiducial values as $w_0 = -0.9$ and $w_1 = -0.8$. As seen from Figs. 7 and 8, the constraints significantly improve when we add information from the 21 cm fluctuations, depending on the values of a_s and p .

First let us discuss the case of $p = 100$. When p is so large, the EoS abruptly changes at the corresponding scale factor a_s (or the redshift z_s). In the case of $a_s = 0.1$ (or

^{#6} The anisotropic stress can also be non-zero if one considers a very general class of dark energy models [83]. However, its effects are not significant either. Hence here we ignore the anisotropic stress of dark energy.

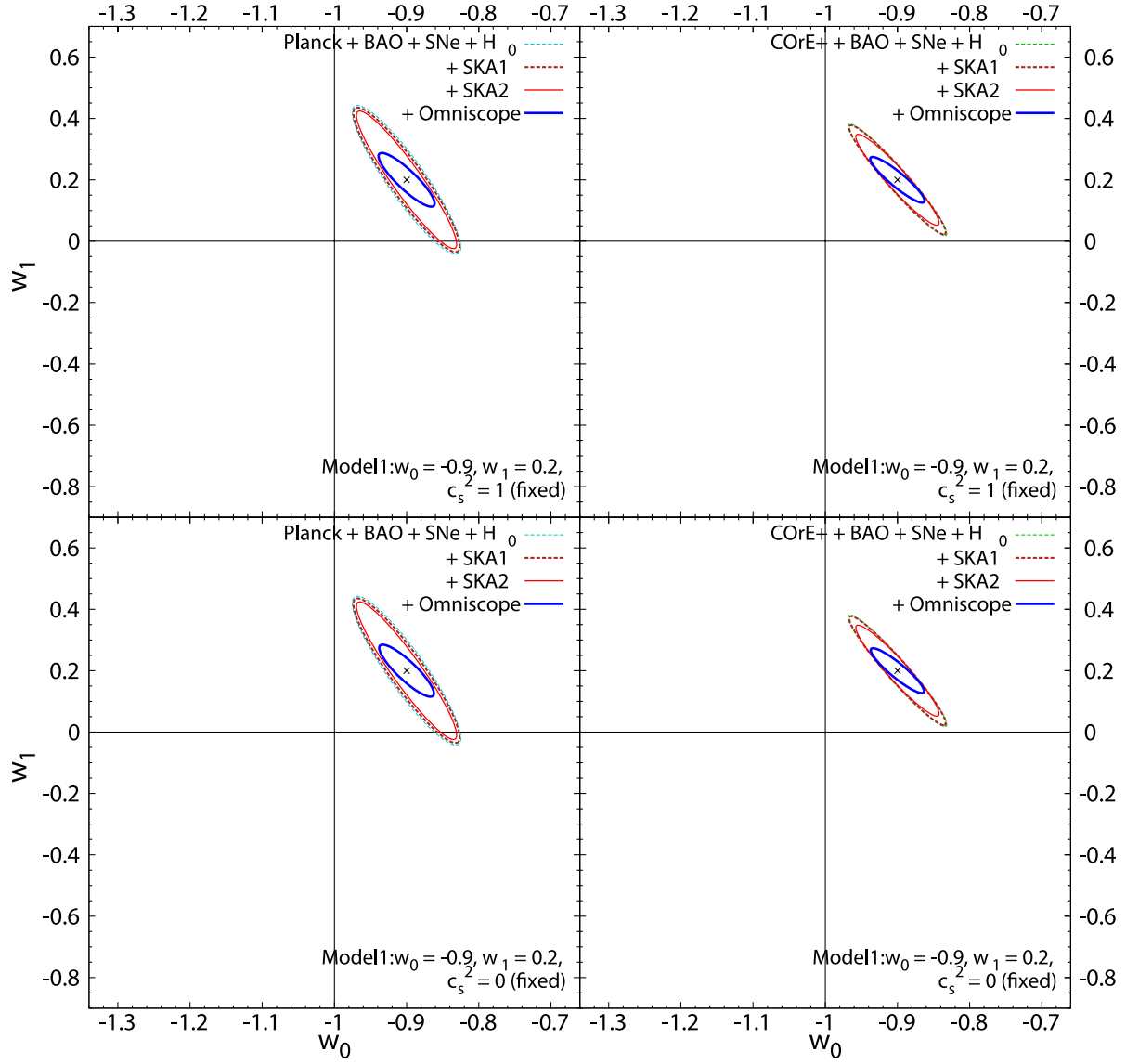


Figure 5: Expected constraints at 95 % C.L. for the parametrization I. We assume $w_0 = -0.9$ and $w_1 = 0.2$ for the fiducial values. Constraints from Planck + BAO + SNe + H_0 with SKA or Omniscope (left panel) and CoRE+ + BAO + SNe + H_0 with SKA or Omniscope (right panel) are shown. The sound speed is taken to be $c_s^2 = 1$ (top panels) and 0 (bottom panels), respectively.

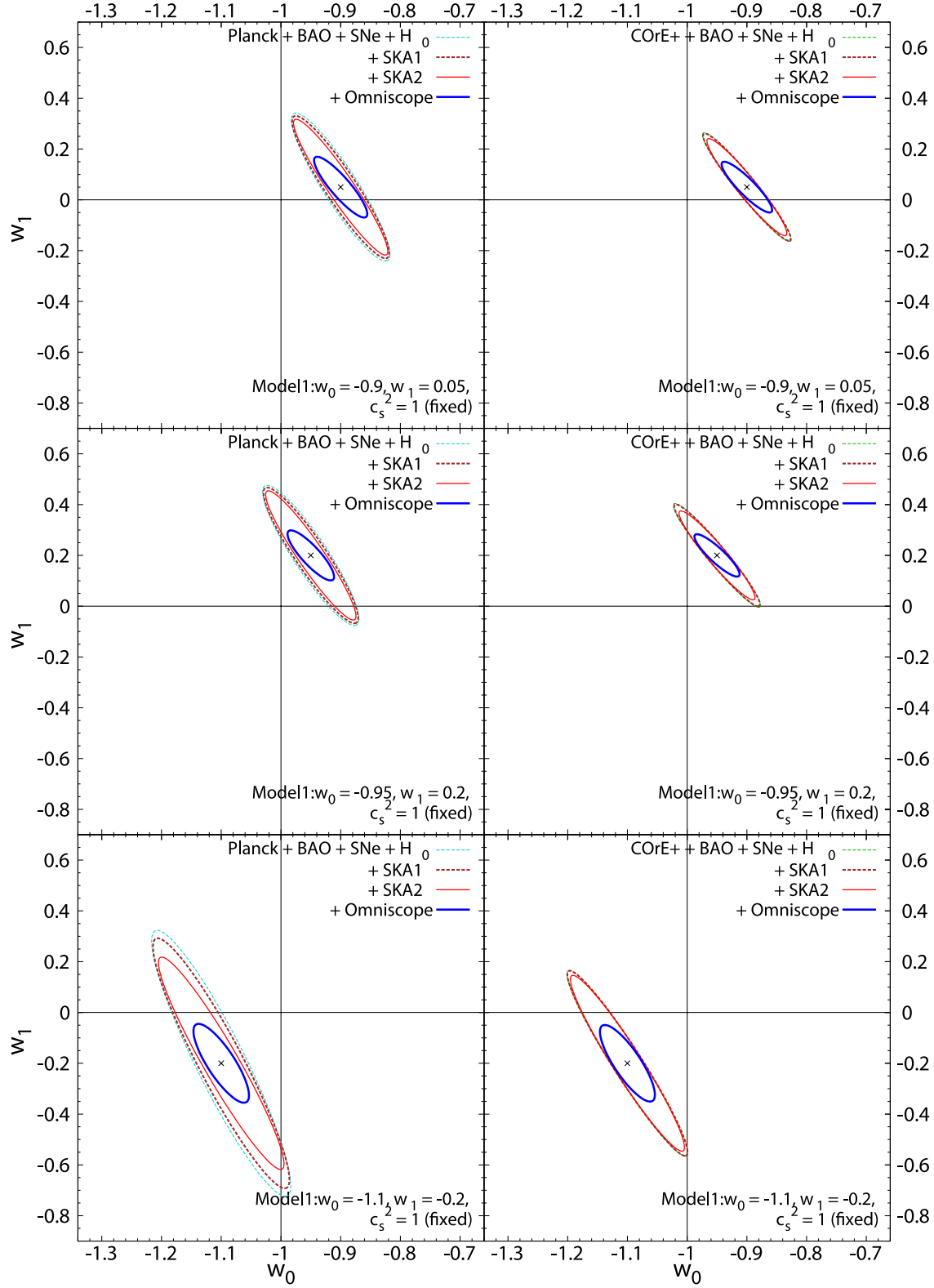


Figure 6: Expected constraints at 95 % C.L. for the parametrization I for the fiducial values of $(w_0, w_1) = (-0.9, 0.05)$ (top), $(-0.95, 0.2)$ (middle) and $(-1.1, -0.2)$ (bottom). In this figure, we fix the sound speed to be $c_s^2 = 1$.

$z_s = 9$) shown in the bottom panel of Fig. 7, the EoS is almost unchanged after $z = 9$. Since BAO and SNe only probe low redshift ($z \lesssim 2$), they are sensitive to the EoS at low redshift. That is why w_1 cannot be determined for the case with the fiducial value of $a_s = 0.1$ with CMB+BAO+SNe+ H_0 . It should be noted here that CMB is not so powerful to constrain the EoS compared to BAO and SNe since integrated quantities such as the angular diameter distance to last scattering surface are the main probes. However CMB is very important to determine the other cosmological parameters which can break some degeneracies among the parameters including the dark energy EoS. Also, for the case with $a_s = 0.25$ (or $z_s = 3$), the data set of CMB+BAO+SNe+ H_0 cannot well determine w_1 . In these cases however, when we add information of 21 cm fluctuations which probes the redshift $6.8 \leq z \leq 10$, w_1 can be severely constrained. This shows the power of the 21 cm observations to investigate dark energy. In the case of $a_s = 0.5$, the EoS changes from w_1 to w_0 at $z_s \sim 1$. Therefore, by the observations of BAO and SNe, we can constrain both of w_0 and w_1 . However even in this case, when we include SKA2, the constraint on w_1 slightly improves. When Omniscope is included, the constraint becomes more severe.

Next let us consider the case of $p = 1$, which is shown in Fig. 8. Then, the EoS changes slowly from w_1 to w_0 . Hence even when the transition redshift is higher than $z = 2$, w_1 can be constrained severely by low-redshift observations like BAO and SNe. A slow change of the EoS also indicates that both of w_0 and w_1 can be well probed at higher redshift, irrespective of the transition redshift z_s . Therefore, the 21 cm observations always improve the constraints in every case for $p = 1$ as shown in Fig. 8.

Now we discuss the constraints on the w_0 - a_s plane in the cases of $p = 100$ and $p = 1$ in Figs. 9 and 10, respectively. For the case of $p = 100$, the 21 cm observations significantly improve the constraints when the transition redshift is high such as $a_s = 0.1$ and 0.25 as those in the w_0 - w_1 plane. For the case of $p = 1$, the tendency is also the same as those in the w_0 - w_1 plane discussed above.

Regarding the parametrization II, the observations of 21 cm fluctuations significantly improve the constraints when the transition redshift is high or the EoS changes slowly.

4.4.3 Parametrization III

This parametrization includes only two parameters, w_0 and b . Hence we show constraints expected from future 21cm and other observations in the w_0 - b plane in Figs. 11 and 12. For the fiducial values, we have assumed $w_0 = -0.9$ and $b = 0.05$ in Fig. 11, and $w_0 = -0.98$ and $b = 0.1$ in Fig. 12, which are inside the allowed region of the current constraint presented in the previous section. The effective sound speed is taken to be $c_s^2 = 1$ or 0 .

As discussed in Section 2, this parametrization is suitable to describe the so-called early dark energy model, in which the effects of the dark energy perturbation can be more significant than those in other parametrizations. However, as one can see from the figure, the constraints for $c_s^2 = 1$ and 0 are almost the same, which indicates that the information on the background evolution mostly determines the constraints. Similarly to the parametrization I, the inclusion of the 21 cm fluctuations do not much improve

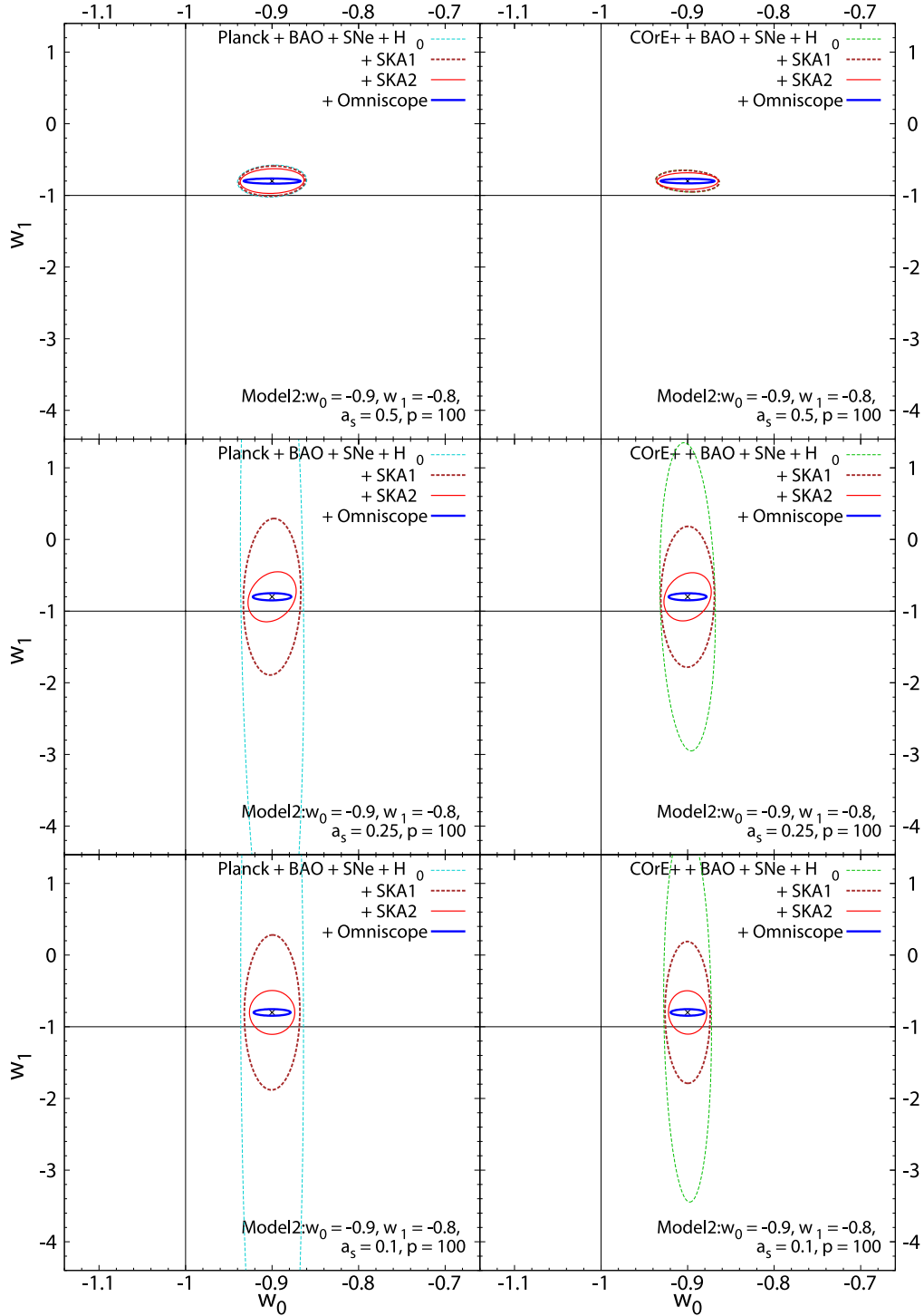


Figure 7: Expected constraints at 95 % C.L. on the w_0 - w_1 plane for the parametrization II. The fiducial values are taken to be $w_0 = -0.9$ and $w_1 = -0.8$. Other EoS parameters are assumed as $a_s = 0.5$ (top panels), 0.25 (middle panels), 0.1 (bottom panels) and $p = 100$. All parameters except w_0 and w_1 are marginalized over. In the left and right panels, Planck and CoRE+ are assumed for CMB, respectively.

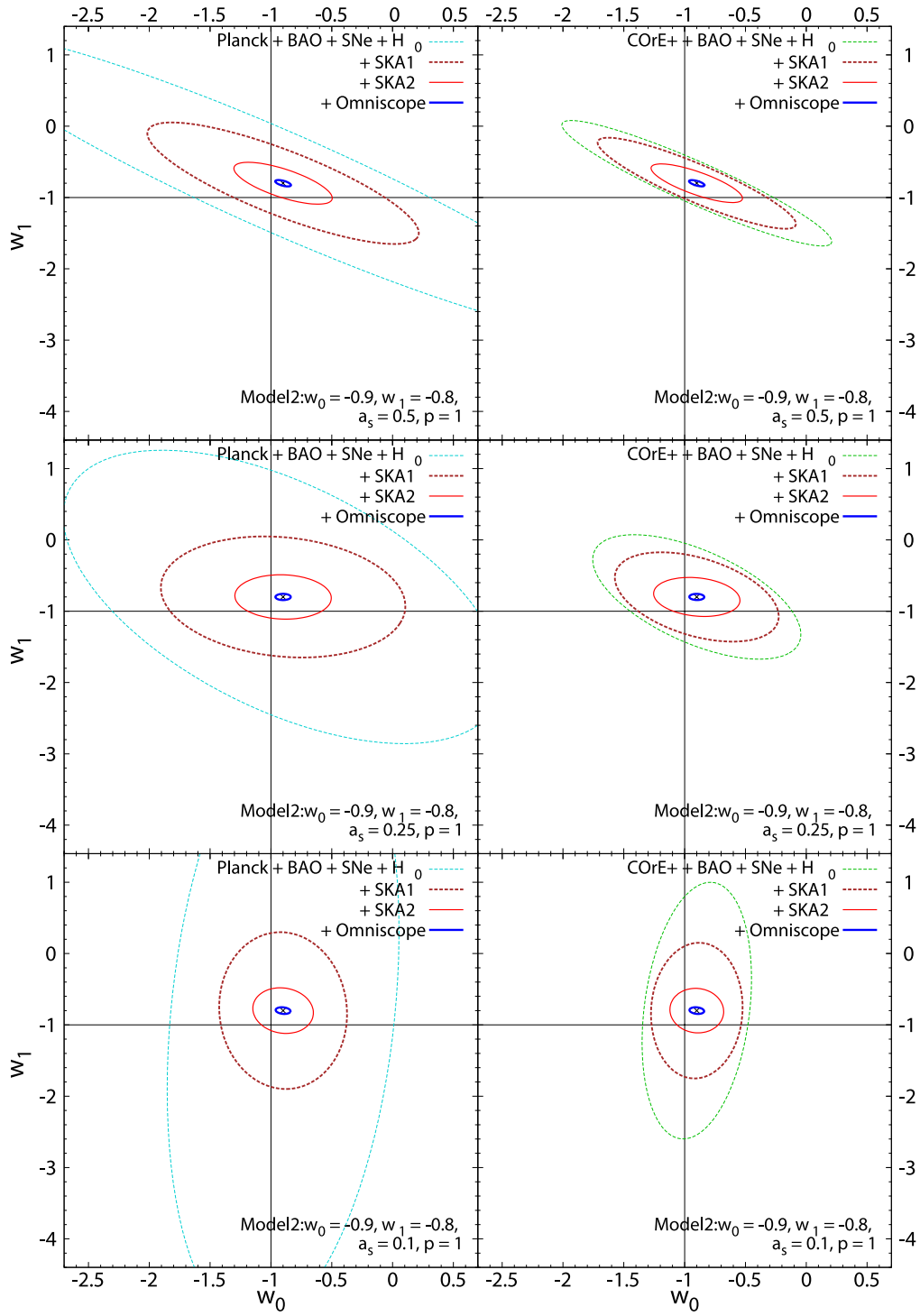


Figure 8: The same as Fig. 7 but for $p = 1$.

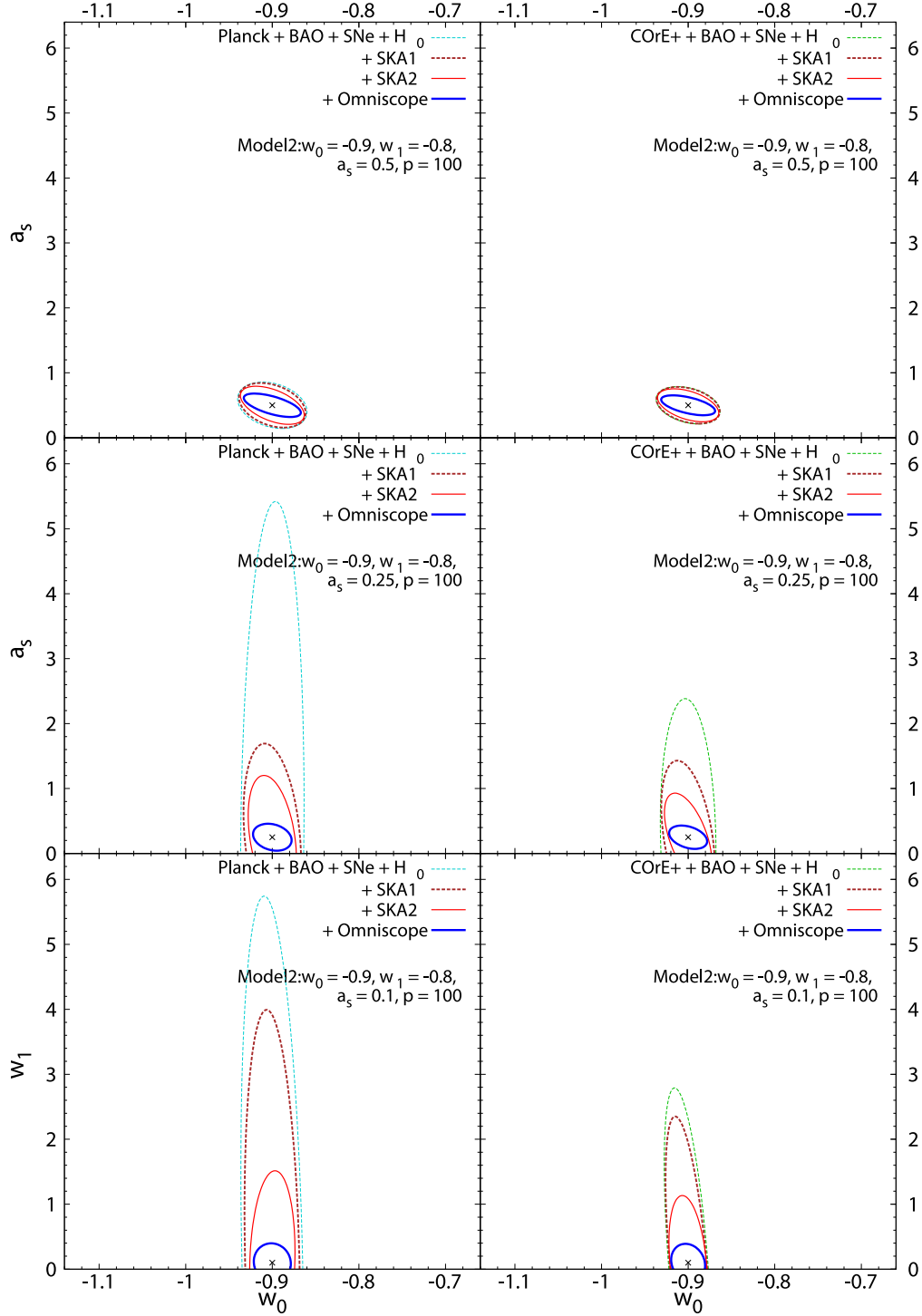


Figure 9: Expected constraints at 95 % C.L. on the w_0 - a_s plane for the parametrization II. For the fiducial values, we assume $(w_0, w_1) = (-0.9, -0.8)$ and $a_s = 0.5$ (top panels), 0.25 (middle panels), 0.1 (bottom panels) and $p = 100$. All parameters except w_0 and a_s are marginalized over. In deriving these constraints, w_1 is marginalized over.

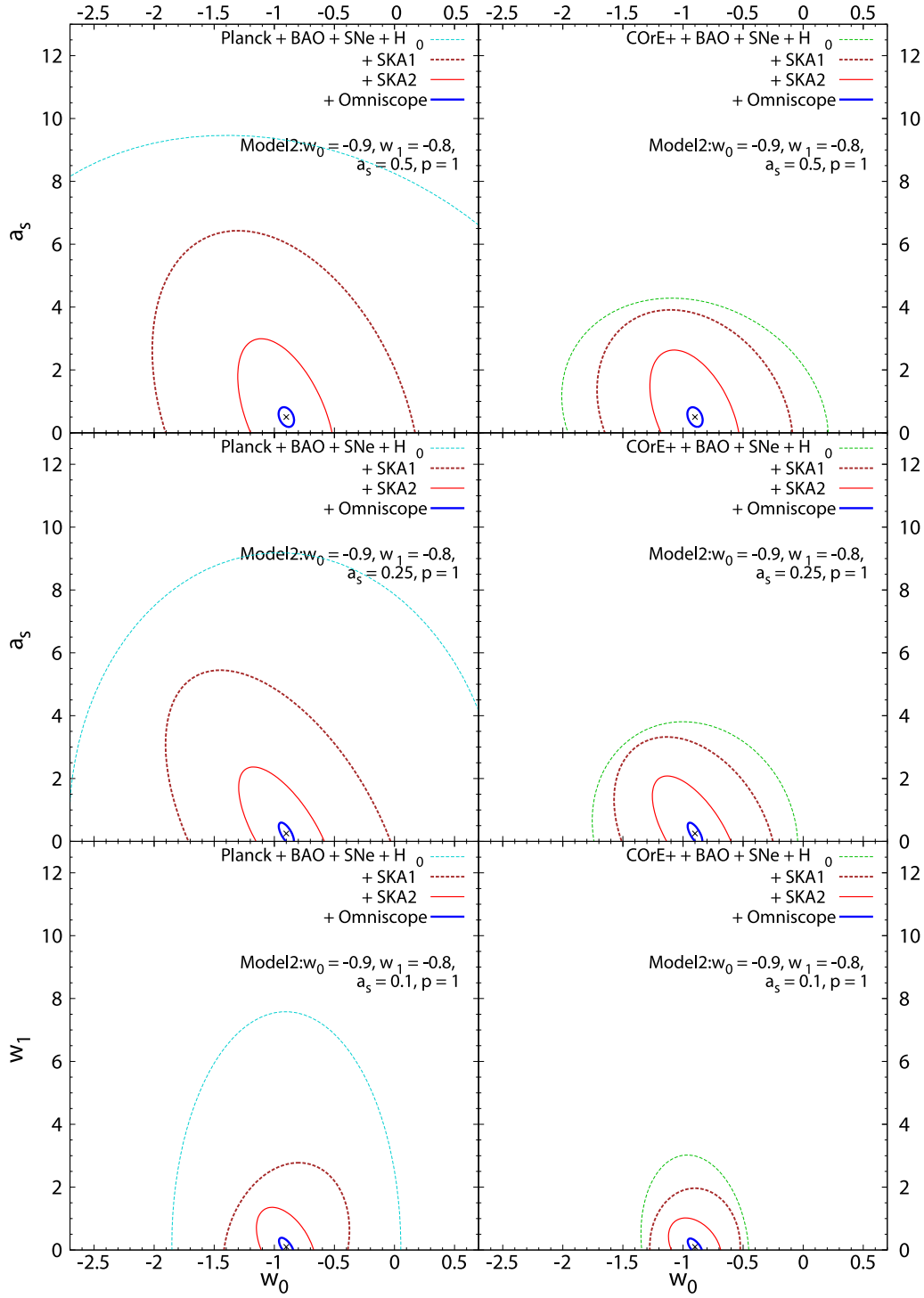


Figure 10: The same as Fig. 9 but for $p = 1$.

Model		CMB+BAO+SNe+ H_0	+ SKA1	+ SKA2	+ Omniscope
Parametrization I	w_0	2.76×10^{-2}	2.70×10^{-2}	2.32×10^{-2}	1.52×10^{-2}
	w_1	7.34×10^{-2}	7.17×10^{-2}	5.97×10^{-2}	3.00×10^{-2}
Parametrization II $(p, a_s) = (100, 0.1)$	w_0	1.11×10^{-2}	1.05×10^{-2}	8.93×10^{-3}	7.90×10^{-3}
	w_1	1.07	3.99×10^{-1}	1.22×10^{-1}	1.84×10^{-2}
Parametrization II $(p, a_s) = (100, 0.25)$	w_0	1.29×10^{-2}	1.25×10^{-2}	1.10×10^{-2}	8.85×10^{-3}
	w_1	8.67×10^{-1}	3.96×10^{-1}	1.36×10^{-1}	1.99×10^{-2}
Parametrization III	w_0	2.49×10^{-2}	2.43×10^{-2}	2.05×10^{-2}	1.37×10^{-2}
	b	2.80×10^{-2}	2.72×10^{-2}	2.20×10^{-2}	1.04×10^{-2}

Table 2: Summary of the expected 1σ errors. For CMB, we adopt the specification of COrE+. The fiducial values for the EoS parameters are assumed to be $(w_0, w_1) = (-0.9, 0.2)$ for Parametrization I, $(w_0, w_1) = (-0.9, -0.8)$ for Parametrization II, $(w_0, b) = (-0.9, 0.05)$ for Parametrization III, and the effective sound speed is fixed as $c_s^2 = 1$.

the constraints at the level of SKA. However, when Omniscope is taken into account, the constraints become more severe, which shows potential of the 21cm fluctuations as a probe of dark energy.

5 Conclusion and discussion

We have investigated expected constraints on dark energy, especially, the parameters which describe the EoS for several dark energy parametrizations using future observations of 21 cm line in combination with CMB, BAO, SNe and H_0 . Since the 21 cm line observations can probe different redshift ranges from CMB, BAO and SNe, they can give more information combined with those other observations. We have assumed the specifications of SKA phase 1, SKA phase 2 and Omniscope for the future 21 cm observations. We have analyzed the three parametrizations for the dark energy equation of state: the parametrization I, II and III. Parametrization I given in Eq. (1) is most commonly used one when the time dependence of the EoS is investigated. Parametrization II (Eq. (3)) can represent the dark energy models which predict a sudden change in the EoS at some redshift. Parametrization III (Eq. (5)) corresponds to the so-called early dark energy model where its EoS gets close to zero as the redshift increases. This feature allows the fraction of the energy density of dark energy can be sizable even at higher redshift.

By assuming these parametrizations, we have studied expected constraints on the parameters in the EoS with and without the future 21 cm observations to see their power to probe the properties of dark energy. We performed the Fisher matrix analysis and have investigated to what extent the future 21 cm observations can improve the constraints on the EoS parameters. We found that a degree of the improvement depends on the parametrization and the fiducial values of the EoS. Table 2 summarizes the expected 1σ bound on the EoS parameters for each parametrizations.

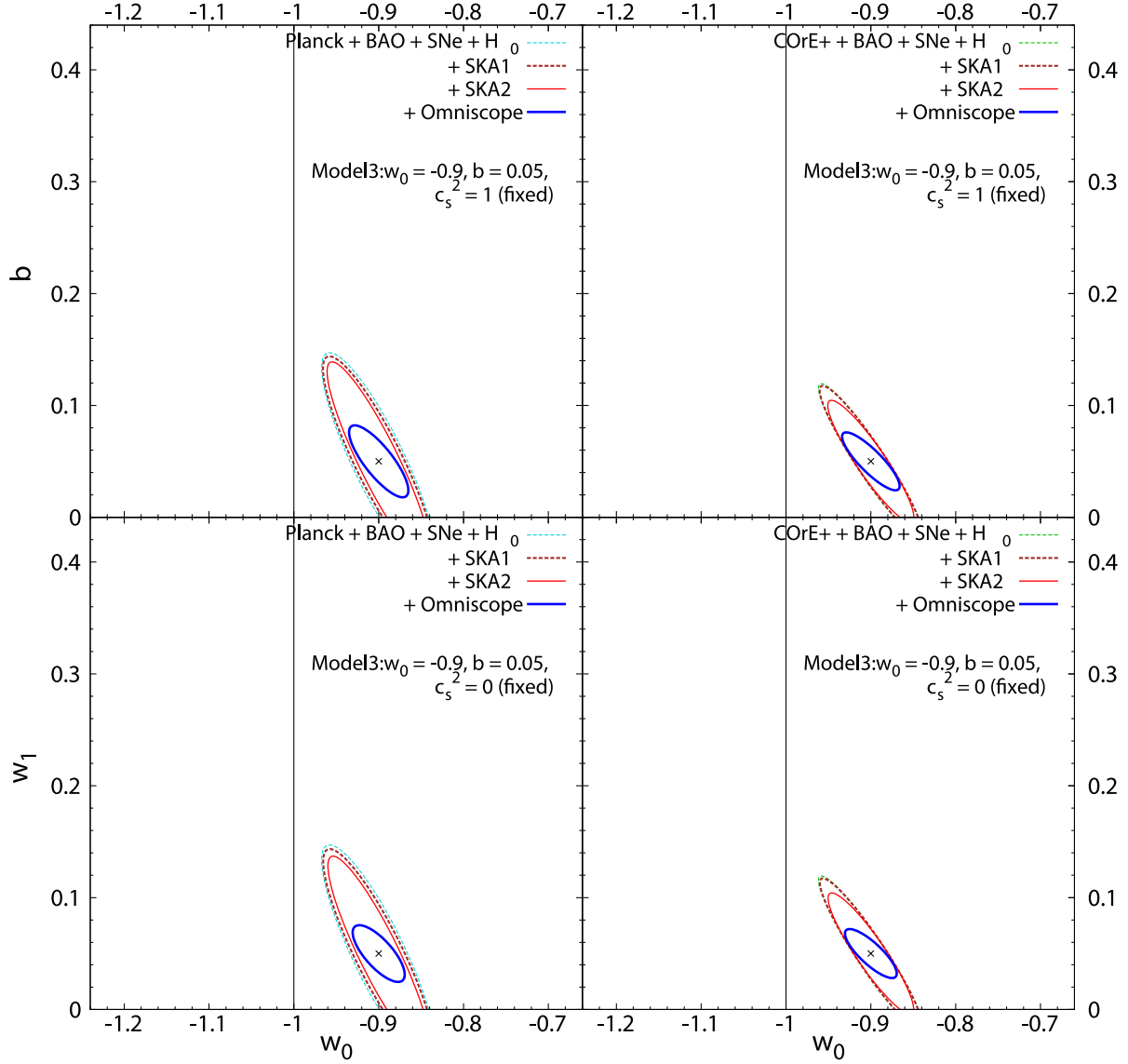


Figure 11: Expected constraints at 95 % C.L. on the w_0 - b plane for the parametrization III. The fiducial values are assumed as $w_0 = -0.9$ and $b = 0.05$. The effective sound speed is fixed to be $c_s^2 = 1$ (top panels) and $c_s^2 = 0$ (bottom panels).

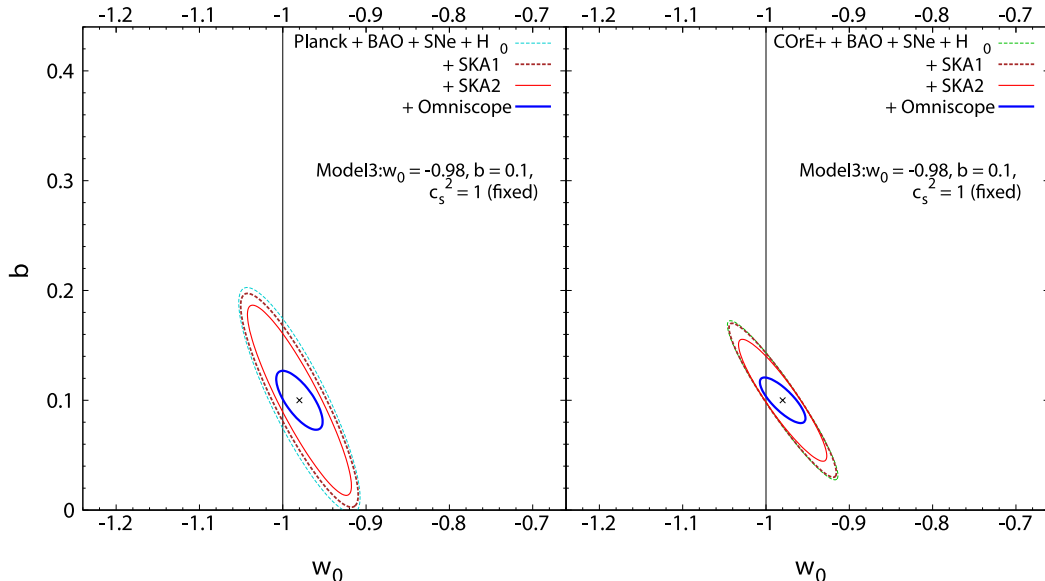


Figure 12: Expected constraints at 95 % C.L. on the w_0 - b plane for the parametrization III for the fiducial values of $(w_0, b) = (-0.98, b = 0.1)$. In this figure, the effective sound speed is fixed to be $c_s^2 = 1$.

For the parametrization I, the inclusion of SKA (even phase 2) does not improve much the constraints. However when Omniscope is combined with CMB+BAO+SNe+ H_0 , the constraints should be significantly improved as clearly shown in Fig. 6.

For the parametrization II, the observations of SKA can significantly improve the constraints on the EoS parameters, depending on the fiducial values. In the parametrization II, the EoS is allowed to change at some redshift from w_1 (the EoS at earlier time) to w_0 (the EoS at later time), which introduces the extra two parameters to describe its evolution: the width and redshift of the transition. When the width of the transition is very narrow, and the transition redshift is high, the observations of BAO and SNe cannot probe the EoS in the earlier time, i.e., w_1 . However, the 21 cm observations can probe higher redshift. Therefore the inclusion of the observations of 21 cm fluctuations can significantly improve the constraints, in particular that for w_1 . However, when the transition redshift is low so that BAO and SNe can probe its change, the constraints from CMB+BAO+SNe+ H_0 are already severe enough. Hence not so much improvement can be made by the 21 cm observations in such a case. These are illustrated in Fig. 7. When the width of the transition is broad, the EoS evolves only gradually, which enables us to probe the EoS in various redshifts. This means that BAO and SNe can always be sensitive to both w_0 and w_1 . Therefore they can be constrained, regardless of the transition redshift without the 21 cm observations. However, as shown in Fig. 8, the constraints can be much improved when the observation of 21 cm is included. We can also see these tendencies by looking at the constraints on the w_0 - a_s plane as shown in Figs. 9 and 10. In constraining dark energy which can be characterized by the parametrization II, the observations of 21

cm fluctuations are very powerful.

For the parametrization III, the tendency is similar to that for the parametrization I. In this parametrization, the 21 cm observations at the level of SKA is not so powerful to improve the constraints. However, when we consider Omniscope-type observations, the determination of the EoS would be much improved, which shows the potential of the 21 cm fluctuations as a probe of this kind of dark energy.

The power of the 21cm line observations may depend on the actual properties of dark energy (i.e., the fiducial value of the EoS parameters and the function form for the time dependence of EoS). Concretely the 21 cm line observations are powerful especially when the EoS of dark energy varies at relatively high redshifts, which are difficult to be probed by other observations. The known key probes such as galaxy-galaxy lensing and redshift-space distortions are definitely important in order to constrain dark energy [74]. Here we would like to stress that the 21cm line observations can be complementary to those probes because the ranges of the observed redshift are much higher. In near future, the so-called next generation of the 21 cm observations such as SKA will become available. Therefore, investigating dark energy with 21 cm is very timely and should be pursued further.

Acknowledgments

This work is partially supported by JSPS KAKENHI Grant Number JP15K05084 (TT), 26247042 (KK), and MEXT KAKENHI Grant Number JP15H05888 (TT), JP15H05889, JP16H0877 (KK). This work was supported by IBS under the project code, IBS-R018-D1 (TS).

A Specifications of observations

	N_{ant}	$A_e (z = 8)$ [m ²]	L_{min} [m]	L_{max} [km]	FoV ($z = 8$) [deg ²]	Obs. time t_0 [hour]	z
SKA phase 1	911/2	443	35	6	13.12×4	1000	6.8 – 10
SKA phase 2	911×4	443	35	6	13.12×4	1000	6.8 – 10
Omniscope	10^6	1	1	1	2.063×10^4	1000	6.8 – 10

Table A.3: Specifications of 21 cm observations for SKA [18] and Omniscope [28]. Note that the effective collecting area A_e and the field of view FoV are proportional to λ^2 , where λ is the observed wave length. However, for Omniscope, we assume that A_e and FoV are fixed. For SKA phase 1 and phase 2, multiple fields are assumed to be observed, and set the number of fields N_{field} to be 4 in our analyses. Then, the effective field of view of SKA phase 1 and phase 2 is $\text{FoV}_{\text{SKA}} = 13.12 \times N_{\text{field}}$ [deg²]. It should be noted that, although we have assumed the number of fields to be 4, our results are almost unchanged even if we change N_{field} for a fixed total observation time. (We have checked this by calculating the expected constraint for different numbers of fields N_{field} and observation time t_0 with the total observation time being fixed (i.e. 4000 hours) and found that expected constraints are almost unchanged by the choice of N_{field} and t_0 .)

Central frequency (GHz)	θ_{FWHM} (arcmin)	Δ_T (μK arcmin)	Δ_P (μK arcmin)
75	14	2.7	4.7
105	10	2.7	4.6
135	7.7	2.6	4.5
165	6.4	2.6	4.6
195	5.4	2.6	4.5
225	4.7	2.6	4.5

Table A.4: Specification of COreE+ [27]. Although there are other channels, we only list those for CMB channels which are used in our analysis.

Central redshift z_i	$\sigma_d(z_i) \times 10^2$	$\sigma_H(z_i) \times 10^2$
0.15	2.78	5.34
0.25	1.87	3.51
0.35	1.45	2.69
0.45	1.19	2.20
0.55	1.01	1.85
0.65	0.87	1.60
0.75	0.77	1.41
0.85	0.76	1.35
0.95	0.88	1.42
1.05	0.91	1.41
1.15	0.91	1.38
1.25	0.91	1.36
1.35	1.00	1.46
1.45	1.17	1.66
1.55	1.50	2.04
1.65	2.36	3.15
1.75	3.62	4.87
1.85	4.79	6.55

Table A.5: Specification of DESI. We reproduce Table 5 in [74] only including the relevant quantities for our analysis. Note that $\sigma_d(z_i)$ and $\sigma_H(z_i)$ are the errors of $\ln(d_A(z_i))$ and $\ln(H(z_i))$, respectively.

z_{\max}	1.7	1.6	1.5	1.4	1.3	1.2	1.1	1.0	
z_{\min}	1.6	1.5	1.4	1.3	1.2	1.1	1.0	0.9	
N_i	136	136	136	136	136	136	136	136	
z_{\max}	0.9	0.8	0.7	0.6	0.5	0.4	0.3	0.2	0.1
z_{\min}	0.8	0.7	0.6	0.5	0.4	0.3	0.2	0.1	0.03
N_i	136	136	136	326	223	402	208	69	800

Table A.6: The number of SNe for each bin assumed in our analysis, which is adopted in [82] for WFIRST-AFTA. In the same manner as presented in the report [82], we include a “near sample” of 800 SNe and the last bin corresponds to it. The low redshift supernovae are observed by ground based experiments, and we assume that their statistical, and systematic errors are the same as those in the far sample. For the statistical errors, we assume $\sigma_{m,i} = 0.08$, $\sigma_D = 0.09$ and $\sigma_{\text{lens},i} = 0.07 \times \bar{z}_i$.

References

- [1] For review, see, e.g., L. Amendola and S. Tsujikawa, “*Dark Energy: Theory and Observations*,” Cambridge University Press (2011); M. J. Mortonson, D. H. Weinberg and M. White, arXiv:1401.0046 [astro-ph.CO].
- [2] For review, see, e.g., T. Clifton, P. G. Ferreira, A. Padilla and C. Skordis, Phys. Rept. **513**, 1 (2012) [arXiv:1106.2476 [astro-ph.CO]]; K. Koyama, arXiv:1504.04623 [astro-ph.CO].
- [3] G. Gubitosi, F. Piazza and F. Vernizzi, JCAP **1302**, 032 (2013) [arXiv:1210.0201 [hep-th]].
- [4] J. Gleyzes, D. Langlois, F. Piazza and F. Vernizzi, JCAP **1308**, 025 (2013) [arXiv:1304.4840 [hep-th]].
- [5] J. K. Bloomfield, É. É. Flanagan, M. Park and S. Watson, JCAP **1308**, 010 (2013) [arXiv:1211.7054 [astro-ph.CO]].
- [6] C. Ringeval, T. Suyama, T. Takahashi, M. Yamaguchi and S. Yokoyama, Phys. Rev. Lett. **105**, 121301 (2010) [arXiv:1006.0368 [astro-ph.CO]].
- [7] D. Glavan, T. Prokopec and D. C. van der Woude, Phys. Rev. D **91**, no. 2, 024014 (2015) [arXiv:1408.4705 [gr-qc]].
- [8] H. Aoki and S. Iso, PTEP **2015**, no. 11, 113E02 (2015) [arXiv:1411.5129 [gr-qc]].
- [9] D. Glavan, T. Prokopec and T. Takahashi, arXiv:1512.05329 [gr-qc].
- [10] P. A. R. Ade *et al.* [Planck Collaboration], arXiv:1502.01590 [astro-ph.CO].
- [11] H. Qing-Guo and W. Ke, arXiv:1606.05965 [astro-ph.CO].
- [12] L. Hollenstein, D. Sapone, R. Crittenden and B. M. Schaefer, JCAP **0904**, 012 (2009) doi:10.1088/1475-7516/2009/04/012 [arXiv:0902.1494 [astro-ph.CO]].
- [13] F. B. Abdalla, C. Blake and S. Rawlings, Mon. Not. Roy. Astron. Soc. **401**, 743 (2010) doi:10.1111/j.1365-2966.2009.15704.x [arXiv:0905.4311 [astro-ph.CO]].
- [14] I. Debono, A. Rassat, A. Refregier, A. Amara and T. Kitching, Mon. Not. Roy. Astron. Soc. **404**, 110 (2010) doi:10.1111/j.1365-2966.2010.16284.x [arXiv:0911.3448 [astro-ph.CO]].
- [15] L. Santos, P. Cabella, A. Balbi and N. Vittorio, Phys. Rev. D **88**, no. 4, 043505 (2013) doi:10.1103/PhysRevD.88.043505 [arXiv:1307.2919 [astro-ph.CO]].

- [16] Y. Takeuchi, K. Ichiki, T. Takahashi and M. Yamaguchi, JCAP **1403**, 045 (2014) [arXiv:1401.7031 [astro-ph.CO]].
- [17] J. S.-Y. Leung and Z. Huang, arXiv:1604.07330 [astro-ph.CO].
- [18] <https://www.skatelescope.org>
- [19] P. Bull, P. G. Ferreira, P. Patel and M. G. Santos, Astrophys. J. **803**, no. 1, 21 (2015) [arXiv:1405.1452 [astro-ph.CO]].
- [20] Y. Xu, X. Wang and X. Chen, Astrophys. J. **798**, no. 1, 40 (2015) doi:10.1088/0004-637X/798/1/40 [arXiv:1410.7794 [astro-ph.CO]].
- [21] X. Chen, Int. J. Mod. Phys. A **30**, 1545011 (2015). doi:10.1142/S0217751X15450116
- [22] A. Hossain, S. Thakur, T. G. Sarkar and A. A. Sen, arXiv:1603.02087 [astro-ph.CO].
- [23] G. B. Zhao, D. Bacon, R. Maartens, M. Santos and A. Raccanelli, arXiv:1501.03840 [astro-ph.CO].
- [24] A. Nusser, Mon. Not. Roy. Astron. Soc. **364**, 743 (2005) doi:10.1111/j.1365-2966.2005.09603.x [astro-ph/0410420].
- [25] S. Wyithe, A. Loeb and P. Geil, Mon. Not. Roy. Astron. Soc. **383**, 1195 (2008) doi:10.1111/j.1365-2966.2007.12631.x [arXiv:0709.2955 [astro-ph]].
- [26] J. R. Pritchard and E. Pierpaoli, Phys. Rev. D **78**, 065009 (2008) doi:10.1103/PhysRevD.78.065009 [arXiv:0805.1920 [astro-ph]].
- [27] <http://www.core-mission.org>
- [28] M. Tegmark and M. Zaldarriaga, Phys. Rev. D **82**, 103501 (2010) doi:10.1103/PhysRevD.82.103501 [arXiv:0909.0001 [astro-ph.CO]].
- [29] V. B. Johri and P. K. Rath, Int. J. Mod. Phys. D **16**, 1581 (2007) [astro-ph/0510017].
- [30] M. Chevallier and D. Polarski, Int. J. Mod. Phys. D **10**, 213 (2001) [gr-qc/0009008].
- [31] E. V. Linder, Phys. Rev. Lett. **90**, 091301 (2003) [astro-ph/0208512].
- [32] D. Huterer and M. S. Turner, Phys. Rev. D **64**, 123527 (2001) [astro-ph/0012510].
- [33] J. Weller and A. Albrecht, Phys. Rev. D **65**, 103512 (2002) [astro-ph/0106079].
- [34] P. H. Frampton and T. Takahashi, Phys. Lett. B **557**, 135 (2003) [astro-ph/0211544].
- [35] S. Hannestad and E. Mortsell, JCAP **0409**, 001 (2004) [astro-ph/0407259].
- [36] C. Wetterich, Phys. Lett. B **594**, 17 (2004) [astro-ph/0403289].

- [37] A. Lewis and S. Bridle, Phys. Rev. D **66**, 103511 (2002) doi:10.1103/PhysRevD.66.103511 [astro-ph/0205436].
- [38] N. Aghanim *et al.* [Planck Collaboration], [arXiv:1507.02704 [astro-ph.CO]].
- [39] F. Beutler *et al.*, Mon. Not. Roy. Astron. Soc. **416**, 3017 (2011) [arXiv:1106.3366 [astro-ph.CO]];
- [40] L. Anderson *et al.* [BOSS Collaboration], Mon. Not. Roy. Astron. Soc. **441**, no. 1, 24 (2014) [arXiv:1312.4877 [astro-ph.CO]];
- [41] A. J. Ross, L. Samushia, C. Howlett, W. J. Percival, A. Burden and M. Manera, Mon. Not. Roy. Astron. Soc. **449**, no. 1, 835 (2015) [arXiv:1409.3242 [astro-ph.CO]].
- [42] P. A. R. Ade *et al.* [Planck Collaboration], arXiv:1502.01591 [astro-ph.CO].
- [43] G. Efstathiou, Mon. Not. Roy. Astron. Soc. **440**, no. 2, 1138 (2014) [arXiv:1311.3461 [astro-ph.CO]].
- [44] M. Betoule *et al.* [SDSS Collaboration], Astron. Astrophys. **568**, A22 (2014) [arXiv:1401.4064 [astro-ph.CO]].
- [45] C. Heymans *et al.*, Mon. Not. Roy. Astron. Soc. **427**, 146 (2012) [arXiv:1210.0032 [astro-ph.CO]].
- [46] M. Jaber and A. de la Macorra, arXiv:1604.01442 [astro-ph.CO].
- [47] B. Y. Pu, X. D. Xu, B. Wang and E. Abdalla, Phys. Rev. D **92**, no. 12, 123537 (2015) doi:10.1103/PhysRevD.92.123537 [arXiv:1412.4091 [astro-ph.CO]].
- [48] K. Kohri, Y. Oyama, T. Sekiguchi and T. Takahashi, JCAP **1310**, 065 (2013) [arXiv:1303.1688 [astro-ph.CO]].
- [49] Y. Mao, M. Tegmark, M. McQuinn, M. Zaldarriaga and O. Zahn, Phys. Rev. D **78**, 023529 (2008) doi:10.1103/PhysRevD.78.023529 [arXiv:0802.1710 [astro-ph]].
- [50] M. McQuinn, A. Lidz, O. Zahn, S. Dutta, L. Hernquist and M. Zaldarriaga, Mon. Not. Roy. Astron. Soc. **377**, 1043 (2007) doi:10.1111/j.1365-2966.2007.11489.x [astro-ph/0610094].
- [51] M. McQuinn, L. Hernquist, M. Zaldarriaga and S. Dutta, Mon. Not. Roy. Astron. Soc. **381**, 75 (2007) doi:10.1111/j.1365-2966.2007.12085.x [arXiv:0704.2239 [astro-ph]].
- [52] A. Datta, J. D. Bowman and C. L. Carilli, Astrophys. J. **724**, 526 (2010) doi:10.1088/0004-637X/724/1/526 [arXiv:1005.4071 [astro-ph.CO]].

- [53] H. Vedantham, N. U. Shankar and R. Subrahmanyam, *Astrophys. J.* **745**, 176 (2012) doi:10.1088/0004-637X/745/2/176 [arXiv:1106.1297 [astro-ph.IM]].
- [54] M. F. Morales, B. Hazelton, I. Sullivan and A. Beardsley, *Astrophys. J.* **752**, 137 (2012) doi:10.1088/0004-637X/752/2/137 [arXiv:1202.3830 [astro-ph.IM]].
- [55] A. R. Parsons, J. C. Pober, J. E. Aguirre, C. L. Carilli, D. C. Jacobs and D. F. Moore, *Astrophys. J.* **756**, 165 (2012) doi:10.1088/0004-637X/756/2/165 [arXiv:1204.4749 [astro-ph.IM]].
- [56] C. M. Trott, R. B. Wayth and S. J. Tingay, *Astrophys. J.* **757**, 101 (2012) doi:10.1088/0004-637X/757/1/101 [arXiv:1208.0646 [astro-ph.CO]].
- [57] B. J. Hazelton, M. F. Morales and I. S. Sullivan, *Astrophys. J.* **770**, 156 (2013) doi:10.1088/0004-637X/770/2/156 [arXiv:1301.3126 [astro-ph.IM]].
- [58] N. Thyagarajan *et al.*, *Astrophys. J.* **776**, 6 (2013) doi:10.1088/0004-637X/776/1/6 [arXiv:1308.0565 [astro-ph.CO]].
- [59] A. Liu, A. R. Parsons and C. M. Trott, *Phys. Rev. D* **90**, no. 2, 023018 (2014) doi:10.1103/PhysRevD.90.023018 [arXiv:1404.2596 [astro-ph.CO]].
- [60] A. Liu, A. R. Parsons and C. M. Trott, *Phys. Rev. D* **90**, no. 2, 023019 (2014) doi:10.1103/PhysRevD.90.023019 [arXiv:1404.4372 [astro-ph.CO]].
- [61] N. Thyagarajan *et al.*, *Astrophys. J.* **804**, no. 1, 14 (2015) doi:10.1088/0004-637X/804/1/14 [arXiv:1502.07596 [astro-ph.IM]].
- [62] H. J. Seo and C. M. Hirata, *Mon. Not. Roy. Astron. Soc.* **456**, no. 3, 3142 (2016) doi:10.1093/mnras/stv2806 [arXiv:1508.06503 [astro-ph.CO]].
- [63] A. Loeb and S. Wyithe, *Phys. Rev. Lett.* **100**, 161301 (2008) doi:10.1103/PhysRevLett.100.161301 [arXiv:0801.1677 [astro-ph]].
- [64] S. Wyithe and A. Loeb, *Mon. Not. Roy. Astron. Soc.* **397**, 1926 (2009) doi:10.1111/j.1365-2966.2009.15019.x [arXiv:0808.2323 [astro-ph]].
- [65] E. Visbal, A. Loeb and J. S. B. Wyithe, *JCAP* **0910**, 030 (2009) doi:10.1088/1475-7516/2009/10/030 [arXiv:0812.0419 [astro-ph]].
- [66] <http://lpsc.in2p3.fr/perotto/>.
- [67] T. Okamoto and W. Hu, *Phys. Rev. D* **67**, 083002 (2003) doi:10.1103/PhysRevD.67.083002 [astro-ph/0301031].

- [68] J. A. Rubiño-Martín, on behalf of the CORe+ Collaboration, Highlights of Spanish Astrophysics VIII, Proceedings of the XI Scientific Meeting of the Spanish Astronomical Society held on September 8-12, 2014, in Teruel, Spain. A. J. Cenarro, F. Figueras, C. Hernández-Monteaudo, J. Trujillo Bueno, & L. Valdivielso (eds.), p. 329-334 (2015).
- [69] P. A. R. Ade *et al.* [Planck Collaboration], arXiv:1502.01589 [astro-ph.CO].
- [70] Y. Oyama, K. Kohri and M. Hazumi, JCAP **1602**, no. 02, 008 (2016) [arXiv:1510.03806 [astro-ph.CO]].
- [71] Y. Oyama, arXiv:1510.05161 [astro-ph.CO].
- [72] Y. Oyama and M. Kawasaki, arXiv:1605.09191 [astro-ph.CO].
- [73] H. J. Seo and D. J. Eisenstein, Astrophys. J. **665**, 14 (2007) doi:10.1086/519549 [astro-ph/0701079].
- [74] A. Font-Ribera, P. McDonald, N. Mostek, B. A. Reid, H. J. Seo and A. Slosar, JCAP **1405**, 023 (2014) [arXiv:1308.4164 [astro-ph.CO]].
- [75] <http://desi.lbl.gov/>
- [76] L. M. Macri, K. Z. Stanek, D. Bersier, L. Greenhill and M. Reid, Astrophys. J. **652**, 1133 (2006) [arXiv:astro-ph/0608211].
- [77] A. L. Argon, L. J. Greenhill, M. J. Reid, J. M. Moran and E. M. L. Humphreys, Astrophys. J. **659**, 1040 (2007) [arXiv:astro-ph/0701396].
- [78] L. Greenhill *et al.*, arXiv:0902.4255 [astro-ph.CO].
- [79] W. L. K. Wu, J. Errard, C. Dvorkin, C. L. Kuo, A. T. Lee, P. McDonald, A. Slosar and O. Zahn, Astrophys. J. **788**, 138 (2014) [arXiv:1402.4108 [astro-ph.CO]].
- [80] A. Albrecht, G. Bernstein, R. Cahn, W. L. Freedman, J. Hewitt, W. Hu, J. Huth and M. Kamionkowski *et al.*, astro-ph/0609591.
- [81] J. Frieman, M. Turner and D. Huterer, Ann. Rev. Astron. Astrophys. **46**, 385 (2008) doi:10.1146/annurev.astro.46.060407.145243 [arXiv:0803.0982 [astro-ph]].
- [82] D. Spergel *et al.*, arXiv:1503.03757 [astro-ph.IM].
- [83] K. Ichiki and T. Takahashi, Phys. Rev. D **75**, 123002 (2007) [astro-ph/0703549].